European Journal of Mechanics B/Fluids 63 (2017) 1–8

Contents lists available at ScienceDirect

European Journal of Mechanics B/Fluids

journal homepage: www.elsevier.com/locate/ejmflu

# Constricted channel flow with different cross-section shapes

A. Van Hirtum [a,*], B. Wu [a], H. Gao [b], X.Y. Luo [b]

[a] GIPSA-lab, CNRS UMR 5216, Grenoble University, France

[b] School of Mathematics and Statistics, University of Glasgow, Glasgow G12 8QW, United Kingdom

ARTICLE INFO

*Article history:*
Received 6 November 2015
Received in revised form
24 November 2016
Accepted 22 December 2016
Available online 12 January 2017

*Keywords:*
Analytical model
Numerical simulation
Experimental validation
Moderate Reynolds number flow

ABSTRACT

Pressure driven steady flow through a uniform circular channel containing a constricted portion is a common problem considering physiological flows such as underlying human speech sound production. The influence of the constriction's cross-section shape (circle, ellipse, circular sector) on the flow within and downstream from the constriction is experimentally quantified. An analytical boundary layer flow model is proposed which takes into account the hydraulic diameter of the cross-section shape. Comparison of the model outcome with experimental and three-dimensional numerically simulated flow data shows that the pressure distribution within the constriction can be modeled accurately so that the model is of interest for analytical models of fluid–structure interaction without the assumption of two-dimensional flow.



## 1. Introduction

Pressure driven channel flow is associated with physiological flows for which constricted channel portions occur either naturally or due to a pathology. Well-known examples are airflow through the human airways (speech production, asthma, obstructive sleep apnea) or blood flow through a stenosis. Physical studies of these flows often rely on mechanical replicas aiming to reproduce phenomena experimentally in a repeatable and controllable way. Such replicas allow a systematic investigation of the potential effect of geometrical parameters on the flow. In the case of human speech production, a partly constricted channel is used as mechanical replica representing a severe simplification of portions of the larynx and vocal tract, see *e.g.* [1–6]. The potential impact of the constriction degree and streamwise position of the constricted channel portion is evaluated whereas the impact of the cross-section shape is not considered. Indeed, in [1–6] a rectangular cross-section shape is used for which the spanwise dimension is not varied. Data obtained when mounting mechanical replicas to a suitable experimental setup are than used in order to validate flow models. In the case of speech production and even more general in the case of physiological flows [7,8], simplified analytical flow models are often sought since they favor to assess the impact of well defined and physiologically meaningful input parameters. In the following we consider flow and geometrical configurations relevant to physical studies of human speech production.

Simplifications of the flow model through the constricted channel geometry are based on a non-dimensional analysis of the governing Navier–Stokes equations [9]. Accounting for typical values of physiological, geometrical and flow characteristics observed on human speakers [10,11,3] result in non-dimensional numbers which allows one to assume the flow through the human upper airways during speech production as incompressible [Mach number, $Ma^2 \ll 0.1$], laminar [Reynolds number $Re \approx O(10^3)$], quasi-steady [Strouhal number $Sr \ll 1$] and two-dimensional (2D) given the channel's mean aspect ratio ($Ar \geq 4$) corresponding to the width-to-height ratio of the rectangular cross-section [2,12,6]. Based on these assumptions, quasi-2D or 2D flow models [13–15] derived from boundary layer theory [9] have proven to be extremely useful to capture the underlying physics and are applied to mimic and predict ongoing phenomena using few computational resources while allowing experimental validation on mechanical replicas. Nevertheless, the assumption of a 2D geometry implies that details of the cross-section shape perpendicular to the streamwise flow direction ($x$) are neglected whereas medical imaging studies of the human upper airway during speech production reveal a large variation of the cross-section shape within the larynx as well as within the vocal tract [10,11].

Previous studies (see *e.g.* [2,13,14]) have shown that in order to represent the flow observed on mechanical replicas of the human upper airway, the contribution of viscous effects to the model outcome is essential. Since viscous effects depend on the cross-section shape [9], adding the constriction's cross-section shape to the set

* Corresponding author.
*E-mail address:* annemie.vanhirtum@grenoble-inp.fr (A. Van Hirtum).

http://dx.doi.org/10.1016/j.euromechflu.2016.12.009

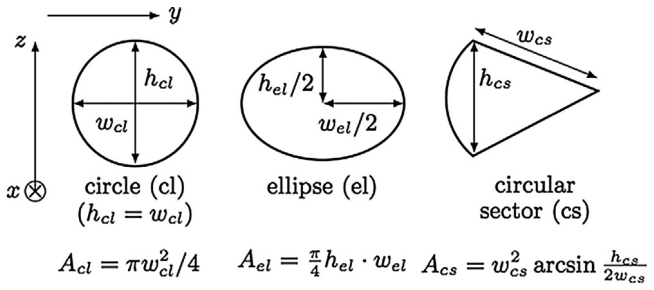


**Fig. 1.** Schematic front view ($(y, z)$ plane) and area $A$ for circle (cl), ellipse (el) and circular sector (cs). Spanwise extent $w$ ($y$-direction) and transverse extent $h$ ($z$-direction) are indicated.

of flow model input parameters is likely to alter the model outcome. Concretely, this implies that the common assumption of 2D flow is not made whereas other flow assumptions, *i.e.* incompressible, laminar and quasi-steady are still valid. Nevertheless, experimental evidence of the influence of the constriction's cross-section shape on mechanical replicas is lacking.

Therefore, in the current work it is aimed firstly to provide experimental evidence of the impact of the cross-section shape on main flow quantities for a mechanical replica pertinent to represent an upper airway constriction during speech sound production [1,6,14]. The mechanical replica has a uniform constriction of constant area but variable cross-section as depicted in Fig. 1. Secondly, it is aimed to propose and validate an analytical laminar boundary layer flow model against measured flow quantities. Furthermore, the outcome of the laminar flow model is compared to numerically simulated data describing laminar three-dimensional flow. Simulated data are obtained using the immersed boundary (IB) method [16] since it is commonly used to describe fluid–structure interactions such as occurring during human speech sound production [17]. Consequently, modeled flow data are compared with measured as well as simulated flow data. Note that for fluid–structure interaction applications such as vocal fold auto-oscillations during voiced speech production, accurate estimation of the pressure within the constriction ($x_1 \leq x \leq x_2$) is most important since it determines the forces exerted by the fluid on the enveloping walls.

In the following, a simplified analytical boundary layer flow model is presented accounting for the cross-section shape by means of its hydraulic diameter. Next, the immersed boundary method to obtain 3D flow simulations is detailed. After that, the experimental setup used to characterize the flow field (velocity and pressure) of the mechanical replica is detailed. Then, results are presented. At first, the impact of the cross-section on measured flow data is shown and the quasi-3D flow model is discussed with respect to experimental observations. Subsequently, a quantitative comparison between measured, modeled and simulated flow data is presented. Finally, a conclusion is formulated.

## 2. Laminar boundary layer flow model

Flow through a uniform circular flow channel of area $A_0$ containing a constriction of constant length $L_c$ and with minimum area $A_c$ is considered as illustrated in Fig. 2. All sharp edges are rounded (measured radius $r = 0.05$ cm). Rounding outlet edges with such a small curvature radius will avoid occurrence of the so-called Coanda effect which is not the case when the constriction outlet is more divergent [9]. Rounding leading edges at the inlet of the constriction aims to reduce a potential vena contracta effect in comparison with sharp inlet edges. Consequently, rounded edges allow to focus on the impact of the cross-section area by reducing other effects related to the constriction geometry. Finally, it is noted that with respect to physiological flow applications rounded edges are more pertinent.

Flow through the constricted channel is then generated by imposing upstream pressure $P_0$ and hence the total driving pressure difference $\Delta P = P_0 - P_d$ where downstream pressure $P_d = 0$. Downstream from the constriction jet formation occurs at the downstream end of the constricted region ($x = x_2 - r$) so that the jet has a finite potential core $x_{pc}$ due to flow mixing and subsequent pressure recovery as depicted in Fig. 2. The impact of the wall curvature of the trailing portion of the constriction on flow separation is neglected since the wall curvature radius of the assessed cross-section shapes (Fig. 1) is much smaller (factor 5 or more) than the overall spanwise or transverse extent (see *e.g.* $w_{\cdot}$ and $h_{\cdot}$ in Table 1). The pressure distribution $P(x, t)$ along the channel ($x_0 \leq x$) is sought.

Boundary layer development influences the flow of a viscous fluid such as air (kinematic viscosity $\nu = 1.5 \times 10^{-1}$ cm$^2$/s and density $\rho = 1.2 \times 10^{-3}$ g/cm$^3$). The constriction length $L_c$ is assumed much shorter than the entrance length necessary to obtain fully viscous flow (developed boundary layers) for all assessed Reynolds numbers $Re$ [9] so that thin boundary layers envelop the core region of the flow. Therefore, a boundary layer flow model is proposed.

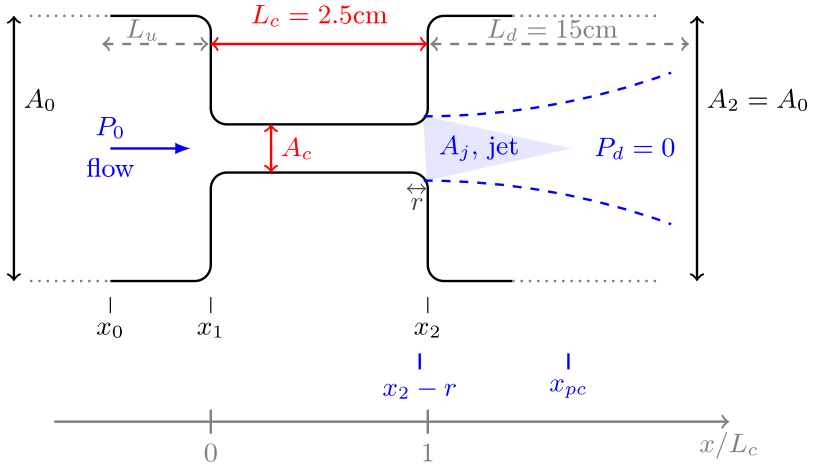


**Fig. 2.** Illustration of pressure driven flow through a uniform circular channel (area $A_0 = 4.9$ cm$^2$) enveloping a constricted portion (area $A_c = 0.79$ cm$^2$ and length $L_c = 2.5$ cm) for which the cross-section shape can be varied (Fig. 1). All sharp edges are rounded (measured radius $r = 0.05$ cm). Main streamwise direction $x$, pressure upstream from the constriction $P_0$, pressure downstream from the constriction $P_d$, upstream unconstricted channel portion length ($L_u$) and downstream unconstricted channel portion length ($L_d = 15$ cm) are indicated. A developing jet (dashed curved lines) of area $A_j$ with finite potential core extent $x_{pc}$ (shaded area) is depicted.

**Table 1**
Overview of geometrical constriction parameters (see Fig. 1): hydraulic diameter $D$, spanwise length $w$, transverse length $h$, cross-section area $A_c$ and constriction length $L_c$. Subscripts ($cl$, $el$, $cs$) are omitted for simplicity.

| | Circle | Ellipse | Circular sector |
|---|---|---|---|
| $D$ (cm) | 1 | 0.67 | 0.72 |
| $w$ (cm) | 1 | 2.24 | 1.73 |
| $h$ (cm) | 1 | 0.45 | 0.9 |

$A_c = 0.79$ cm$^2$, $L_c = 2.5$ cm.

The flow is assumed steady, laminar and incompressible and the no-slip boundary condition is applied on the channel walls as is volume flow rate conservation $d\Phi/dx = 0$, with volume flow rate $\Phi$. Flow separation and jet formation are assumed to occur at the end of the constricted portion. Pressure recovery due to flow mixing of the jet issued from the constriction with the surrounding fluid downstream from the constriction is then modeled using conservation of mass and momentum over the mixing region:

$$u_j A_j = u_2 A_2, \tag{1}$$

$$\rho u_2^2 A_2 = P_j A_2 + \rho A_j u_j, \tag{2}$$

where subindex $j$ and 2 indicate respectively the jet region (cross-sectional area $A_j$, velocity $u_j$ and pressure $P_j$) and the region downstream from the mixing zone (cross-sectional area $A_2 = A_0$, velocity $u_2$ and pressure $P_2 = P_d = 0$). The jet cross-sectional area is given as

$$\frac{A_j}{A_c} = \left(1 - \frac{2\delta_1}{D}\right)^2 \quad \text{or} \quad \frac{A_j}{A_c} \approx 1 - \frac{4\delta_1}{D} \text{ since } \frac{2\delta_1}{D} < 1, \tag{3}$$

with $\delta_1$ the displacement thickness of the boundary layer approximated as the value for a flat plate of length $L_c$ associated with a Blasius velocity profile [9]:

$$\delta_1 \approx 1.7\sqrt{\frac{L_c D}{Re_{ref}}}, \tag{4}$$

where reference Reynolds number $Re_{ref} = \frac{D u_{ref}}{\nu}$ is defined using hydraulic diameter $D$ and reference velocity $u_{ref} = \sqrt{\frac{2P_0}{\rho}}$. An estimation of the pressure within the jet $P_j$ yields

$$\frac{P_j}{P_0} = \frac{-2\frac{A_j}{A_2}\left(1 - \frac{A_j}{A_2}\right)}{1 - \frac{2A_j}{A_2}\left(1 - \frac{A_j}{A_2}\right)} \tag{5}$$

and the pressure drop $\Delta P_c = P_c - P_j$ becomes

$$\frac{\Delta P_c}{P_0} = \frac{P_0 - P_j}{P_0}\left(1 - \frac{A_j^2}{A_c^2}\right). \tag{6}$$

The pressure within the constriction is given as $P(0 \le x \le L_c) \approx P_j + \frac{x\Delta P_c}{L_c}$ so that the pressure at the center ($x/L_c = 0.5$) of the constriction is approximated as $P_1 \approx P_j + \frac{\Delta P_c}{2}$.

The centerline velocity $u$ within the constriction ($0 \le x \le L_c$), *i.e.* in the core flow region outside the boundary layer, is estimated by approximating the area $A(x)$ following (3) and (4) as

$$\frac{A(x)}{A_c} = \left(1 - \frac{2\delta_1(x)}{D}\right)^2 \quad \text{with } \delta_1(x) \approx 1.7\sqrt{\frac{xD}{Re_{ref}}} \tag{7}$$

so that

$$u(x) \approx \frac{\Phi}{A(x)} \tag{8}$$

with volume flow velocity $\Phi$ estimated as

$$\Phi \approx u_{ref} \cdot \overline{A(x)}, \tag{9}$$

where $\overline{A(x)}$ indicates the mean value of $A(x)$ within the constriction using (7).

The velocity downstream from the constriction within the potential core ($L_c < x \le x_{pc}$) is assumed constant so that $u(x) \approx \frac{\Phi}{A_j}$ holds. The velocity decay downstream from the potential core is not modeled. Finally, the bulk velocity in the unconstricted tube portion is approximated as $u_b = \frac{\Phi}{A_0}$. Consequently, $u \approx u_b$ is assumed to provide the velocity upstream from the constriction and downstream from the jet's decay region, *i.e.* near the channel exit.

## 3. Numerical 3D flow simulation

Pressure-driven incompressible laminar air flow through a constricted channel as depicted in Fig. 2 is considered. An adaptive immersed boundary (IB) method is used for the simulations [16]. IB uses a Lagrangian description of the immersed structure, along with an Eulerian description of the momentum, velocity, and incompressibility of the coupled fluid–structure system. In brief, let $\Omega \subset \mathbb{R}^3$ denote the physical domain occupied by the fluid–structure system. Let $\mathbf{x} = (x, y, z) \in \Omega$ denote fixed physical coordinates, and $U \subset \mathbb{R}^3$ denotes the reference coordinate system attached to the channel structure, described by $\mathbf{X} = (X, Y, Z) \in U$, which are the material coordinates. Then at time $t$, the physical position of material point $\mathbf{X}$ can be described as $\boldsymbol{\chi}(\mathbf{X}, t)$, therefore, $\boldsymbol{\chi}(U, t) = \Omega_s$ is the occupied region by the channel structure. The fluid region at time $t$ is $\Omega_f(t) = \Omega \setminus \Omega_s$. The IB formulation of the equations [16] is:

$$\rho\left(\frac{\partial \mathbf{u}}{\partial t}(\mathbf{x}, t) + \mathbf{u}(\mathbf{x}, t) \cdot \nabla \mathbf{u}(\mathbf{x}, t)\right) = -\nabla p(\mathbf{x}, t) + \mu \nabla^2 \mathbf{u}(\mathbf{x}, t) + \mathbf{f}(\mathbf{x}, t), \tag{10}$$

$$\nabla \cdot \mathbf{u}(\mathbf{x}, t) = 0, \tag{11}$$

$$\frac{\partial \boldsymbol{\chi}}{\partial t}(\mathbf{X}, t) = \int_\Omega \mathbf{u}(\mathbf{x}, t)\, \delta(\mathbf{x} - \boldsymbol{\chi}(\mathbf{X}, t))\, \mathrm{d}\mathbf{x}, \tag{12}$$

$$\mathbf{f}(\mathbf{x}, t) = \int_U \mathbf{F}(\mathbf{X}, t) \delta(\mathbf{x} - \boldsymbol{\chi}(\mathbf{X}, t)) \mathrm{d}\mathbf{X} \tag{13}$$

where $\mathbf{u}(\mathbf{x}, t)$ is the Eulerian fluid velocity field, $p(\mathbf{x}, t)$ is the Eulerian pressure field, $\mathbf{f}(\mathbf{x}, t)$ is the Eulerian elastic force density, $\mathbf{F}(\mathbf{X}, t)$ is the Lagrangian elastic force density, which relates to the mechanics of the immersed channel structure, and $\delta(\mathbf{x}) = \delta(x)\,\delta(y)\,\delta(z)$ is the three-dimensional Dirac delta function. As the immersed channel structure is rigid, this is modeled by applying a tethering force

$$\mathbf{f}_{\text{tether}} = k\,(\boldsymbol{\chi}(\mathbf{X}, t) - \mathbf{X}), \tag{14}$$

where we choose the parameter $k = 10$ N/cm. This will ensure that the structure is anchored in place. We further assume that $\mathbf{f}(\mathbf{x}, t)$ only comes from the tethering force because the structure deformation is negligible. Hence $\mathbf{F}(\mathbf{X}, t) = \mathbf{f}_{\text{tether}}$.

The flow channel (Fig. 2) used for numerical simulations has a total length of 22.5 cm with radius 1.25 cm at its inlet and outlet which corresponds to area $A_0 = 4.9$ cm$^2$. The constricted portion has length $L_c = 2.5$ cm and cross-sectional area $A_c = 0.79$ cm$^2$ so that the constriction degree yields 84%. The unconstricted upstream portion has length $L_u = 5$ cm (or $2 \times L_c$) and the unconstricted downstream portion has length $L_d = 15$ cm (or $6 \times L_c$). All sharp edges are rounded (radius $r = 0.05$ cm) as depicted in Fig. 2. The channel walls are rigid as expressed by the parameter $k$

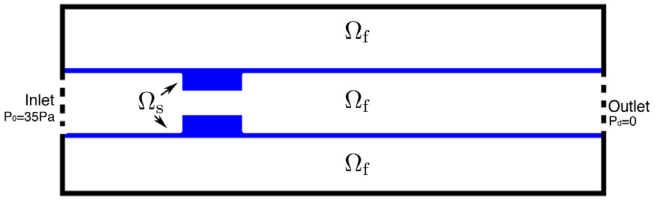


**Fig. 3.** Schematic illustrating the immersed boundary model of the flow channel. $\Omega_s$ is the wall, $\Omega_f$ is the fluid domain.

and have a thickness of 0.1 cm. A geometrical model of the channel structure is generated (SolidWorks CAD) and converted into a mesh with 204 862 tetrahedron elements [18].

The flow channel is immersed in a rectangular 22.5 cm × 5.4 cm × 5.4 cm fluid box, as shown in Fig. 3. The discretization of the fluid box is initialized with a $N \times N \times N$ Cartesian grid for $N = 128$ resulting in a grid size within the constriction of 0.4 mm in the spanwise and transverse direction, and 1.7 mm in the streamwise direction. The numerical treatment of the employed IB method is detailed in [19]. In brief, a staggered-grid discretization of the velocity **u** and force fields **f** is used, whose components are approximated at the center of the Cartesian cell faces to which that component is normal. The pressure field $p$ is approximated at the center of the cells. The divergence, gradient, and Laplace operators are approximated using standard second-order accurate finite difference methods. A version of the piecewise parabolic method is used to discretize the convective term. An explicit version of Crank Nicolson–Adams Bashforth scheme is employed for time stepping, which requires a relatively small time step size ($2.5e^{-6}$ s) in our simulations. This hybrid version of IB scheme is implemented within the open-source IBAMR software framework (https://github.com/IBAMR/IBAMR), which provides an adaptive and distributed-memory parallel infrastructure for developing fluid–structure interaction models which use IB method. A pressure gradient is prescribed between the inlet ($x/L_c = 2$) and outlet ($x/L_c = 7$) of the interior part of the flow channel, i.e. $P_0 - P_d$ with $P_d = 0$ Pa (Figs. 3 and 2), whereas zero pressure boundary conditions are employed along the remainder of the fluid domain boundary. Simulations are performed for steady flow with $P_0 = 35$ Pa.

The total simulation time is about 50 ms, statistical convergence is obtained after 20 ms. Grid independence is tested with fluid grids of 100 × 100 × 100, 128 × 128 × 128, and 128 × 128 × 160. The maximum velocity difference at $t = 20$ ms are less than 3% between the last two grids. Since the grids of 128 × 128 × 128 requires less computational time compared to the finest grids, all the results from the grids with 128 × 128 × 128 are used in the following. Statistical quantities are derived on 10 ms of simulated flow field. Except when stated differently, mean flow results are plotted.

Fig. 4 shows the flow patterns at 40 and 50 ms for both velocity and pressure. It can be seen that the flow is in a transitional regime. The flow in the nozzle region is laminar, after exiting from the nozzle, the flow gradually transits in to turbulence, although the finest scales of the turbulence cannot be captured without involving the turbulence modeling.

In order to study the effect of cross-sectional shape (circle, ellipse, elliptical sector in Fig. 1), all other geometrical parameters are constant ($L_c = 2.5$ cm and $A_c = 0.79$ cm$^2$). Concrete values of geometrical characteristics (spanwise length $w_.$, transverse length $h_.$) indicated in Fig. 1 for the circle, ellipse and circular sector (with opening angle of 30°) are summarized in Table 1. In addition, the associated hydraulic diameter $D = 4A/P$, proportional to the ratio of cross-sectional area $A$ and its wetted perimeter $P$ [20], is given. From the magnitude of the hydraulic diameter $D$ and assuming similar $\Phi$ and $A_c$, the bulk Reynolds number $Re = \frac{\Phi D}{\nu A_c}$ associated

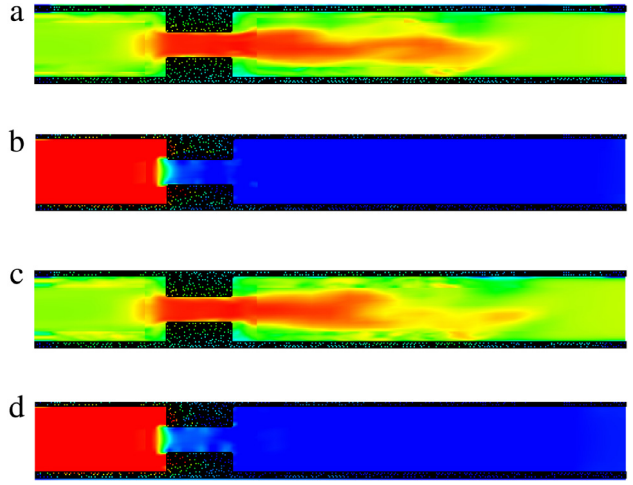


**Fig. 4.** Illustration of instantaneous flow velocity (a) and pressure (b) patterns at 40 ms, and instantaneous flow velocity (c) and pressure (d) patterns at 50 ms. Blue to red represents values from low to high. (For interpretation of the references to color in this figure legend, the reader is referred to the web version of this article.)

with the different cross-sections can be listed in descending order as circle, ellipse and circular sector. Therefore, following a reasoning based on decreasing Reynolds number, viscous effects are likely to be most notable for the circular sector [9].

## 4. Experimental setup

### 4.1. Constricted channel with different cross-section shape

Experiments are performed for three different constrictions so that the cross-section is either a circle, an ellipse or a circular sector. In order to validate the outcome of the modeled and simulated flow, constriction geometries assessed in numerical simulation are reconstructed using Rapid prototyping (ProJet 3510 SD with accuracy <0.01 cm). Reconstructed constrictions are illustrated in Fig. 5. The cross-section is positioned in the $(y, z)$ plane where as before $y$ denotes the spanwise and $z$ the transverse direction. In comparison with the numerical grid, the constriction's streamwise extrema are prolonged in order to add screwthread (Fig. 5) so that an upstream and downstream circular tube with area $A_0 = 4.9$ cm$^2$ (or diameter $D_0 = 2.5$ cm so that $L_c = 1 \times D_0$) can be attached airtightly. Consequently, the constriction degree of the flow channel yields again 84%. The downstream tube has length $L_d = 15$ cm ($\approx 7 \times D_0$) as was the case for numerical simulations. The upstream tube on the other hand has length $L_u = 5$ cm ($\approx 2 \times D_0$) in the numerical grid whereas the length of the downstream tube used in the experiments yields $L_u = 100$ cm ($\approx 50 \times D_0$) in order to favor laminar flow at the inlet of the constriction during the experiments [9].

### 4.2. Flow facility

The experimental setup, depicted in Fig. 6, consists of an air compressor (Atlas Copco GA7), followed by a pressure regulator (Norgren type 11-818-987) providing an airflow at constant pressure. The volume flow rate $\Phi$ is controlled by a manual valve placed downstream from the pressure regulator. Its value is measured by a thermal mass flow meter (Model 4043 TSI) with an accuracy of 2% of its reading. Flow experiments are performed for volume rates within the range $0 < \Phi \leq 3333$ cm$^3$/s. The increment yields 83 cm$^3$/s for $\Phi \leq 1333$ cm$^3$/s, 166 cm$^3$/s for 1500 cm$^3$/s $\leq \Phi \leq$ 1666 cm$^3$/s and 416 cm$^3$/s for $\Phi \geq$ 2083 cm$^3$/s. To homogenize the flow, a settling chamber is used,

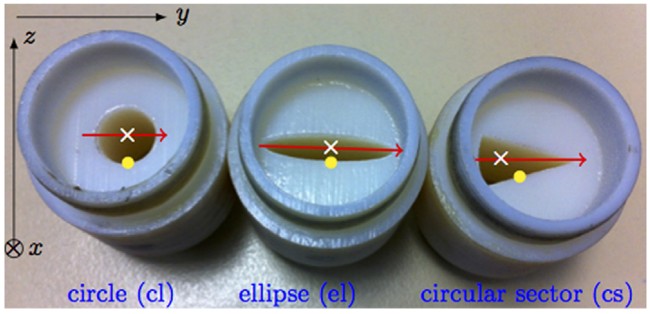


**Fig. 5.** Illustration of reconstructed uniform constrictions with different cross-sectional shapes ($(y, z)$ plane) as depicted in Fig. 1. Position of pressure tap $P_1$ (•) and direction of velocity profiles along the major axis (⟶, spanwise profiles) are depicted. The cross-sectional position (×) of longitudinal velocity profiles is indicated as well.

with dimensions 25 cm × 30 cm × 35 cm, to which a series of 3 perforated plates with holes of diameter 0.15 cm are added. The walls of the settling chamber are tapered with acoustic foam (SE50-AL-ML Elastomeres Solutions) in order to avoid acoustic resonances. The influence of the cross-section shape on the flow development is assessed experimentally by adding the constricted flow channel containing one of the reconstructed constrictions (Fig. 5) to the settling chamber by means of a converging nozzle as depicted in Fig. 6. The used nozzle is designed so that the resulting nozzle flow is laminar for the assessed range of volume flow rates $\Phi \leq 3333$ cm$^3$/s [21]. Except for the air compressor, the whole setup is placed in a confined room in order to avoid flow disturbances.

### 4.3. Steady flow measurements: pressure and velocity

Pressure sensors (Kulite XCS-093) can be positioned in pressure taps of diameter 0.04 cm so that the pressure upstream from the constriction $P_0$, within the constriction $P_1$ and near the flow channel's exit $P_2$ can be measured as illustrated in Fig. 6. Pressure tap $P_1$ is located in the center of the constricted portion at $x/L_c = 0.5$ in order to avoid pressure measurements in the region near the upstream trailing edge of the constriction where the flow field is potentially affected by a vena contracta effect [9]. The position of the pressure tap $P_1$ in the cross-sectional $(y, z)$-plane is detailed in Fig. 5. Electrical signals are amplified and conditioned using an input/output data acquisition system consisting of a pre-amplifier/conditioning board (National Instruments SXCI-1121) connected to a PC through a National Instruments BNC-2080 and a National Instruments PCI-MIO-16XE acquisition card. The acquired data are processed using LabView 7 software (National Instruments). Volume flow rate $\Phi$ and pressure $P_{0,1,2}$ are sampled at 500 Hz and 24 kHz, respectively. Statistical quantities, such as mean values, are derived on 5 s of steady signal for the measured volume flow rate $\Phi(t)$ and pressure signal $P(t)$ [18].

The flow velocity downstream from the constriction is measured for each of the assessed reconstructed constriction geometries (Fig. 5) by hot film anemometry as illustrated in Fig. 7. The hot film (TSI 1201-20) is mounted to a positioning system with accuracy of 0.01 cm [18]. The probe displacement is controlled by a user-defined matrix implemented in LabView (National Instruments) using the input–output data acquisition system. At each spatial measurement position, the hot-film output voltage is sampled at 10 kHz during 40 s by a constant temperature anemometer system (TSI IFA 300). Following calibration of the hot-film, statistical quantities such as the mean and root mean square velocity are derived at each measurement position [22].

Spanwise velocity profiles are gathered by positioning the hot film at a distance <0.1 cm downstream from the center of the nozzle exit and displacing the hot film with a spanwise step of 0.05 cm parallel to the cross-section exit plane across the direction depicted in Fig. 5. Longitudinal velocity profiles in the near field downstream from the constriction for elliptical and circular sector cross-section shape are obtained by positioning the hot film at a distance <0.1 cm downstream from the nozzle exit at the cross-sectional position associated with the centerline of the jet, *i.e.* $(w_{cl}/2, h_{cl}/2)$ for circle, $(w_{el}/2, h_{el}/2)$ for ellipse and $(w_{cs} \times 0.3, h_{cs}/2)$ for circular sector as illustrated in Fig. 5 [20,18]. Next, the hot film is displaced with streamwise steps of 0.2 cm up to 3 cm downstream from its initial position followed by a streamwise step of 0.5 cm up to 16 cm from its initial position ($\Delta x = 16$ cm in Fig. 7). For the flow channel with circular constriction, the longitudinal velocity is measured with the constriction's inlet with steps of 0.2 cm up to 6 cm downstream from its initial position followed by a streamwise step of 0.5 cm up to 18.5 cm from its initial position ($\Delta x = 18.5$ cm in Fig. 7).

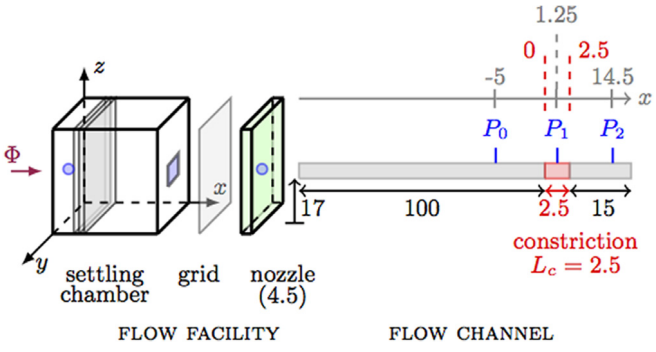


**Fig. 6.** Schematic overview (dimensions in (cm)) of elements of the experimental setup for pressure measurements with volume flow rate $\Phi$ and pressure taps: upstream ($P_0$), within the constriction ($P_1$) and near the channel's exit ($P_2$).

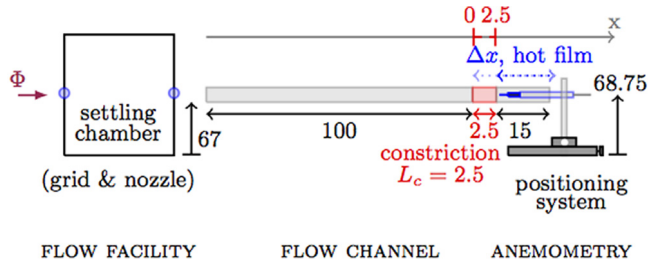


**Fig. 7.** Schematic overview (dimensions in (cm)) of elements of the experimental setup to measure the velocity field immediately downstream from the constriction. The total displacement extents ($\Delta x$ double arrows) of the hot film during longitudinal velocity profiles is indicated ($\Delta x = 16$ cm for ellipse and circular sector and $\Delta x = 18.5$ cm for circle). The position of the jet centerline in the cross-sectional $(y, z)$-plane and the displacement direction associated with spanwise ($y$-axis) velocity profiles is illustrated in Fig. 5.

## 5. Boundary layer flow model validation

Qualitative and quantitative features of the boundary layer flow model are discussed in relation to experimental observations and 3D simulated data. At first, experimental data are considered. It is sought to show the impact of the cross-section shape experimentally as well as to characterize the range of input pressure values for which the flow within the constriction is laminar since laminar flow within the constriction is an assumption underlying the simplified flow model. Next, estimated and measured flow quantities are compared in detail for input pressure $P_0 = 35$ Pa, which will be shown to result in laminar flow within the constriction as was suggested by the simulated flow field.

### 5.1. Experimental data: qualitative model evaluation

#### 5.1.1. Pressure within the constriction

The pressure drop purely due to flow inertia, *i.e.* without viscosity, expressed as ratio $P_x/P_0$ between the pressure somewhere within the uniform portion of the constriction ($P_x = P(x)$ with $x_1 < x < x_2$ in Fig. 2) and upstream from the constriction ($P_0$ at $x = x_0$) depends solely on the geometry as $P_x/P_0 \approx 1 - (A_s/A_c)^2$ with $A_s \approx 0.95$ cm$^2$ and $A_c = 0.79$ cm$^2$ and neglecting $A_0 = 4.9$ cm$^2$ [9]. Therefore, the ratio $P_x/P_0$ is constant within the constricted portion and yields about 145% independently from cross-section shape or applied volume flow rate $\Phi$. Viscosity is expected to reduce this pressure drop. In contrast to the term expressing flow inertia, the viscous term depends on volume flow rate $\Phi$, and hence bulk Reynolds number *Re*, as well as on the cross-section shape [9].

This reasoning fits well with experimental observations of the ratio $P_1/P_0$ (Fig. 8) between mean pressures measured within ($P_1$) and upstream ($P_0$) from the constriction as a function of Reynolds number *Re*. Indeed, it is seen that the pressure drop within the constriction depends on both the cross-section shape and Reynolds number. The maximum pressure drop within the constriction is for all cases (121% for circle, 119% for ellipse and 114% for circular sector) smaller than 145%, the pressure drop associated with purely inertial flow. This confirms that viscosity affects the flow for all three constrictions at a rate determined by the cross-section shape. Moreover, note that the decreased magnitude of pressure drop reduction ordered by cross-section shape (ellipse then circular sector and then circle) is consistent with the increase of hydraulic diameter ($D_{el} < D_{cs} < D_{cl}$, see Table 1) for all Reynolds numbers *Re*.

The initial increase of the pressure drop with Reynolds numbers in the range $0 < Re < Re_t$, with $Re_t$ denoting the Reynolds number associated with maximum pressure drop ($Re_t \approx 6000$ for circle, $Re_t \approx 7000$ for ellipse and $Re_t \approx 6700$ for circular sector), expresses the increasing impact of inertial flow effects compared to viscous flow effects expressed by Reynolds number increase [9]. On the other hand, for Reynolds numbers *Re* greater than $Re_t$ the pressure drop is seen to reduce for all cases (cl, el and cs) indicating that an additional pressure recovery occurs likely due to the transition from laminar to turbulent flow which reduces the pressure drop with about 6% compared to its maximum value (116% for circle, 113% for ellipse and 108% for circular sector). The range of Reynolds numbers associated with the transitional flow regime depends on the cross-section shape as well since pressure recovery occurs *e.g.* more slowly for circle as for circular sector since 4% pressure recovery corresponds to $Re_t + 8000$ compared to $Re_t + 3000$, respectively (Fig. 8). The flow within the constriction remains laminar ($Re \ll Re_t$) for all assessed cross-section shapes as upstream pressure $P_0 < 150$ Pa. The boundary layer flow model is not expected to capture tendencies observed for Reynolds numbers associated with the transitional or turbulent flow regime since laminar flow is assumed within the constriction.

#### 5.1.2. Velocity downstream from the constriction

For the assessed flow channel (Fig. 7), the jet is confined by the downstream tube of 15 cm between $1 \times L_c$ up to $7 \times L_c$ which corresponds to at least 15 times the hydraulic diameter ($15 \times D_{cl}$ for circle, $22 \times D_{el}$ for ellipse and $21 \times D_{cs}$ for circular sector). In this case, the jet is likely to re-attach somewhere along the walls of the downstream tube due to mixing and expansion despite reduced flow entrainment due to confinement [9].

In order to illustrate jet development, the longitudinal velocity profile $u(x)$ is measured along the centerline of the jet (Fig. 2) in the range $1 < x/L_c \leq 7$ (Fig. 7) while imposing upstream pressure $P_0 = 35$ Pa resulting in laminar flow ($Re < Re_t$) within the constriction for all cases since $Re \approx 4200$ for circle, $Re \approx 2800$ for ellipse and $Re \approx 3000$ for circular sector. Measured longitudinal profiles normalized by the reference velocity $u_{ref} = \sqrt{2P_0/\rho}$ are shown in Fig. 9. Immediately downstream from the constriction exit the normalized velocity depends on the flow development within the constriction so that viscous effects – and hence the cross-section shape – contribute to shape the initial jet velocity which varies up to 8%. Note that the observed decrease of initial jet velocity ($u_{el} > u_{cs} > u_{cl}$ at $x/L_c \approx 1$) corresponds to the measured pressure drop increase ($(P_1/P_0)_{el} < (P_1/P_0)_{cs} < (P_1/P_0)_{cl}$ in Fig. 8). The initial velocity is maintained within the potential jet core of finite extent ($x_{pc} \leq 2 \times L_c$). The dynamics of the jet in both the potential core as well as in the decay region further downstream is observed to depend on the velocity field at the constriction exit and therefore on the cross-section shape. Indeed, the potential core extent $x_{pc}$ varies as a function of the cross-section shape of the constriction since its value increases (300%) from the ellipse to the circle ($x_{pc}/L_c = 2.0$ or $x_{pc}/D = 5.0$ for circle, $x_{pc}/L_c = 0.48$ or $x_{pc}/D = 1.8$ for ellipse and $x_{pc}/L_c = 0.88$ or $x_{pc}/D = 3.0$ for circular sector). The decay region of the ellipse exhibits velocity peaks in the range $2 \times L_c < x < 3 \times L_c$ (or $7.5 \times D < x < 11.2 \times D$) indicating axis switching of the jet whereas a continuous velocity decay is observed for the circle and circular sector although at a different rate since the decay is more rapid for circle than for circular sector. The observed velocity decay towards the flow channel's exit ($x/L_c = 7$) motivates the assumption of $P_d = 0$ at the channel's exit, which is confirmed by pressure measurements near the channel's exit, *i.e.* $P_2 = 0 \pm 3$ Pa for $Re < Re_t$.

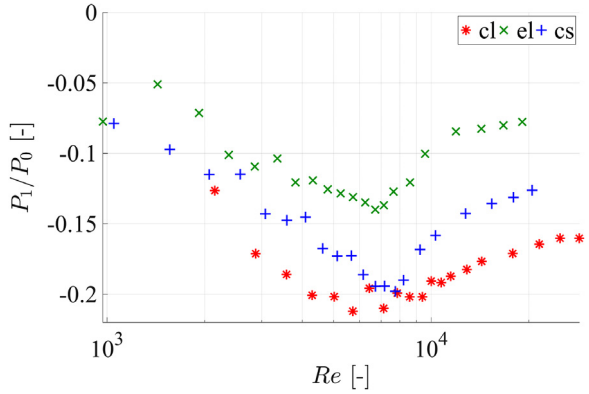


**Fig. 8.** Measured ratio $P_1/P_0$ between mean pressure within ($P_1$) and upstream ($P_0$) from the constriction as a function of Reynolds number *Re* for cross-section shapes: circle (cl−∗), ellipse (el−×) and circular sector (cs−+).

### 5.2. Experimental, modeled and numerical data: quantitative model evaluation for $P_0 = 35$ Pa

The laminar boundary layer flow model takes into account the cross-section shape by means of its hydraulic diameter *D*. The 3D flow simulations rely on a laminar flow description as well and are expected to capture jet expansion mechanisms related to viscosity and the influence of the cross-section shape in more detail. Therefore, in order to evaluate the flow model, it is of interest to compare the model outcome with the simulated flow field as well as with experimental observations within the laminar flow regime ($Re < Re_t$). In the following, a comparison between modeled, simulated and measured flow features is presented for upstream pressure $P_0 = 35$ Pa which is well within the range of upstream pressures ($P_0 < 150$ Pa) for which $Re \ll Re_t$ for all cross-section shapes.

Modeled (subscript *bl*) pressure distributions $P_x$, simulated (subscript *s*) pressure distributions $P_x$ and experimentally (subscript *e*) observed pressures $P_1$ at the center of the constriction

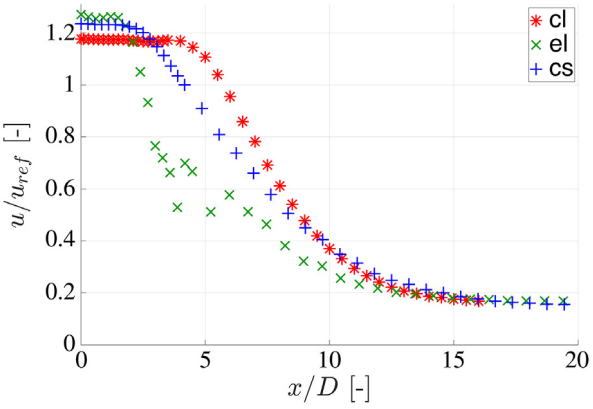


**Fig. 9.** Normalized measured longitudinal mean velocity $u/u_{ref}$ for $P_0 = 35$ Pa downstream from the constriction as a function of streamwise position $x$ normalized by the hydraulic diameter $D$ (Fig. 7) for cross-section shapes: circle (cl—∗), ellipse (el—×) and circular sector (cs—+).

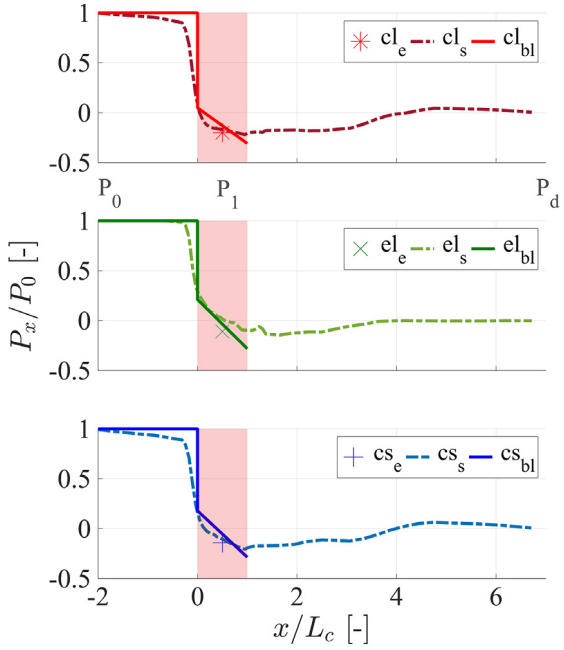


**Fig. 10.** Illustration of modeled (thick full line, subscript *bl*) and simulated (dash-dotted line, subscript *s*) pressure distribution $P_x = P(x)$ normalized by the upstream pressure $P_0 = 35$ Pa at $x/L_c = -2$ for cross-section shapes as a function of streamwise position $x/L_c$: circle (cl—top), ellipse (el—middle) and circular sector (cs—bottom). Measured pressures $P_1$ at $x/L_c = 0.5$ (symbol, subscript *e*) are also shown. The downstream pressure at $x/L_c = 7$ yields $P_d = 0$. The constricted flow channel portion corresponds to the shaded area.

are plotted in Fig. 10 for all assessed cross-section shapes. Modeled (<10%) and simulated (<5%) pressures result in an accurate estimation of the measured pressure drop ($P_1/P_0$) at the center of the constriction ($x/L_c = 0.5$) for all cross-section shapes. In addition, modeled and simulated pressure drops $P_1/P_0$ decrease when the cross-section is varied from ellipse to circular sector and to circle in agreement with experimental observations ($(P_1/P_0)_{el} < (P_1/P_0)_{cs} < (P_1/P_0)_{cl}$ in Fig. 8). Within the constriction ($0 \leq x/L_c \leq 1$) both the modeled and simulated pressure distribution decreases downstream from the constriction's inlet ($x = 0$). In the case of an ideal inviscid flow, the pressure distribution would depend solely on the varying area so that in this case, the pressure distribution would remain constant within the constriction since its area $A_c$ does not change. Accounting for viscosity reduces the pressure drop within the constriction compared to the case of an ideal flow. The magnitude of the pressure drop reduction will depend on the

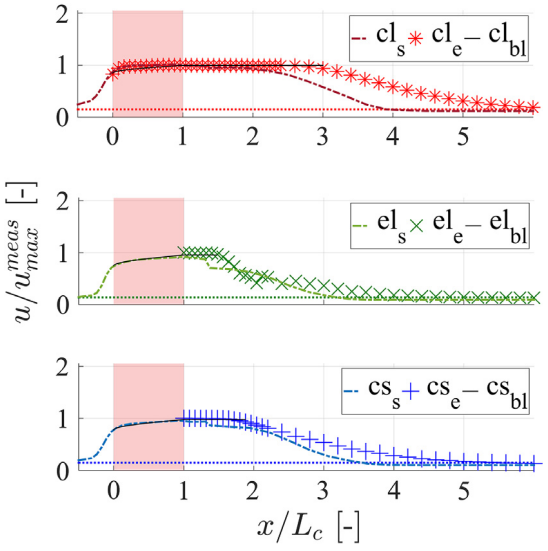


**Fig. 11.** Illustration of simulated (dash-dotted line, subscript *s*) and measured (symbol, subscript *e*) longitudinal velocity profile $u$ along the centerline of the jet (constant cross-sectional $(y, z)$-position as indicated in Fig. 5) normalized by the maximum of the measured profile $u_{max}^{meas}$ as a function of streamwise position $x/L_c$: circle (cl—top), ellipse (el—middle) and circular sector (cs—bottom). The modeled velocity from the constriction inlet up to the end of the potential core (thin full line, subscript *bl*) and bulk velocity $u_b$ (horizontal dotted line) is indicated as well. The constricted flow channel portion corresponds to the shaded area.

cross-section shape as well as on the streamwise extent of the constricted portion. Concretely, at the center of the constricted portion ($x/L_c = 0.5$) the inviscid pressure drop (144%) is reduced to 113% for circle, 104% for ellipse and 106% for circular sector when the boundary layer model is applied. Modeled and 3D simulated pressures within the constriction are in good agreement. At the center of the constriction the simulated pressure yields $116 \pm 9\%$ for circle, $100 \pm 6\%$ for ellipse and $112 \pm 13\%$ for circular sector. Note that the standard derivation around the mean value does not change within the constriction and is of the same order of magnitude as experimentally observed for $P_1$ [18]. The maximum difference (<20%) between modeled and simulated pressure occurs near the inlet and outlet of the constriction suggesting that in these regions the boundary layer model neglects some phenomena, *e.g.* the presence of flow recirculation zones due to the severity of the constriction (constriction degree reduces abruptly with more than 80% at $x = x_1$ in Fig. 2) or asymmetrical boundary layer development in the case of the circular sector [18,20]. Vortex formation, jet expansion and associated recirculation zones affect the simulated pressure distributions downstream from the constriction for all cross-section shapes since negative pressures are observed along the potential core of the simulated jet (up to $x/L_c \approx 3$, Fig. 10) whereas pressure recovery is observed as the flow expands further downstream (downstream from $x/L_c \approx 3$, Fig. 10).

Simulated, measured and modeled longitudinal velocity profiles are shown in Fig. 11. Modeled, simulated and measured velocities within the constriction are in good agreement (overall <5%) for all assessed cross-section shapes. Consequently, both the modeled and simulated velocity provide a fair estimation (<5% for circle and circular sector and <10% for ellipse) of the initial jet velocity at the constriction's exit and therefore of the constant velocity within the potential core. Nevertheless, the potential core extent is underestimated (≈50% when considering constant velocity) when comparing simulated with measured values. The bulk velocity approximates the simulated velocity near the channels inlet and outlet. The standard deviation on the simulated and measured mean velocities within the constriction and within the potential core was less than 5% whereas within the velocity decay region of the jet the variation increases (>15%) [18].

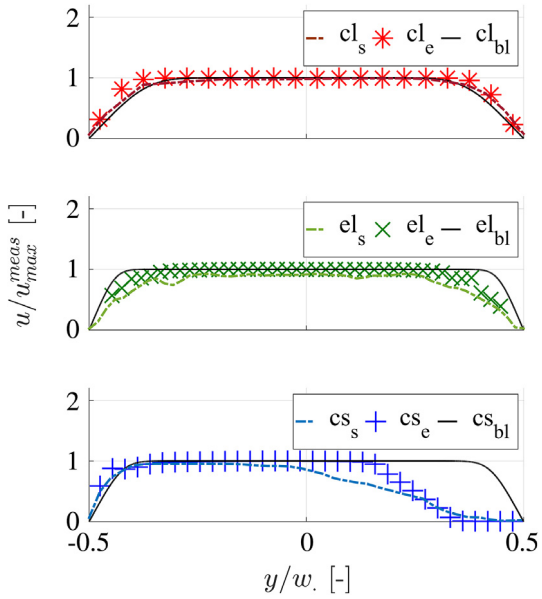


**Fig. 12.** Illustration of simulated (dash-dotted line, subscript *s*) and measured (symbol, subscript *e*) spanwise (see Fig. 5) velocity profiles $u$ normalized by the maximum of the measured profile $u_{\max}^{meas}$ as a function of spanwise position $y/w$ : circle (cl—top), ellipse (el—middle) and circular sector (cs—bottom). The normalized modeled laminar Blasius velocity profile is shown (dashed line, subscript *bl*).

Simulated and measured spanwise velocity profiles are shown in Fig. 12. In general, it is seen that the simulated velocity profile matches well with the measured velocity since it predicts an ideal core flow with constant velocity enveloped by a viscous boundary layer in agreement with experimental observations. Normalized laminar Blasius velocity profiles describing boundary layer development are plotted in Fig. 12 as well [9]. Blasius solution matches measurements in the boundary layer and core region for the circle, again confirming laminar flow within the constriction. Nevertheless, since it does only depends on one spatial dimension, *i.e.* the streamwise dimension, Blasius's profile loses its accuracy as the cross-section geometry becomes more complex. This is best seen for the circular sector as it fails to predict the boundary development for $y/w > 0$.

## 6. Conclusion

Steady pressure-driven flow through a uniform channel containing a constriction with fixed area and length is assessed for different cross-section shapes, *i.e.* circle, ellipse and circular sector. The impact of the cross-section shape is shown experimentally within the constriction (pressure distribution) and for jet development downstream from the constriction (centerline velocity).

An analytical model is proposed which accounts for laminar boundary layer development within the constriction and pressure recovery due to jet mixing downstream from the constriction while considering the cross-section shape by means of its hydraulic diameter so that the assumption of 2D flow is not made. The boundary layer model is evaluated qualitatively and quantitatively by comparing its outcome to measured values as well as to 3D flow simulations. The pressure within the constriction is estimated accurately for all cross-section shapes. In addition, the proposed flow model provides an estimation of the centerline velocity distribution within the constriction. Consequently, the model allows to estimate main flow properties within the constriction at a negligible computational cost as long as the underlying boundary layer assumptions hold.

An analytical solution for flow through a constricted channel of arbitrary shape is of interest for applications where a constriction occurs naturally so that its shape cannot be altered. An example of such an application is the physical study of human speech sound production where such geometries occur within the vocal tract or within the larynx.

Current findings encourage future development of a 3D boundary layer model in order to further increase the model accuracy at a low computational cost.

## Acknowledgments

Authors gratefully acknowledge financial support from EPSRC grant no EP/I029990/1 (UK) and the Explora'Doc program from the Rhône Alpes Region (France). Anonymous reviewers are acknowledged for their comments and suggestions.

## References

[1] C.H. Shadle, The acoustics of fricative consonants. Technical Report, Massachusetts Inst. of Tech., US, 1985.
[2] X. Pelorson, A. Hirschberg, R. Van Hasselt, A. Wijnands, Y. Auregan, Theoretical and experimental study of quasi-steady flow separation within the glottis during phonation. application to a modified two-mass model, J. Acoust. Soc. Am. 96 (6) (1994) 3416–3431.
[3] B.H. Story, I.R. Titze, E.A. Hoffman, Vocal tract area functions from magnetic resonance imaging, J. Acoust. Soc. Am. 100 (1996) 537–554.
[4] A. Barney, C.H. Shadle, P.O.A.L. Davies, Fluid flow in a dynamic mechanical model of the vocal folds and tract. i. measurements and theory, J. Acoust. Soc. Am. 105 (1) (1999) 444–455.
[5] J. Cisonni, A. Van Hirtum, X. Pelorson, J. Willems, Theoretical simulation and experimental validation of inverse quasi one-dimensional steady and unsteady glottal flow models, J. Acoust. Soc. Am. 124 (2008) 535–545.
[6] A. Van Hirtum, X. Pelorson, O. Estienne, H. Bailliet, Experimental validation of flow models for a rigid vocal tract replica, J. Acoust. Soc. Am. 130 (2011) 2128.
[7] Y.C. Fung, Biomechanics Circulation, Springer, 2010.
[8] S. Naili, M. Thiriet, C. Ribreau, Etude tridimensionnelle des contraintes de cisaillement à la paroi dans un tube de section droite non circulaire, C.R. Mèc. 330 (7) (2002) 483–490.
[9] H. Schlichting, K. Gersten, Boundary Layer Theory, seventh ed., Springer, Berlin, 2000.
[10] G. Fant, Acoustic Theory of Speech Production, Mouton & Co., 1960.
[11] R. Daniloff, G. Schuckers, L. Feth, The Physiology of Speech and Hearing, Prentice-Hall, 1980.
[12] J. Cisonni, A. Van Hirtum, X.Y. Luo, X. Pelorson, Experimental validation of quasi-one-dimensional and two-dimensional glottal flow models, Med. Biol. Eng. Comput. 48 (9) (2010) 903–910.
[13] P.Y. Lagree, E. Berger, M. Deverge, C. Vilain, A. Hirschberg, Characterization of the pressure drop in a 2d symmetrical pipe: Some asymptotical, numerical, and experimental comparisons, J. Appl. Math. Mech. / Z. Angew. Math. Mech. 85 (2) (2005) 141–146.
[14] C.E. Vilain, X. Pelorson, C. Fraysse, M. Deverge, A. Hirschberg, J. Willems, Experimental validation of a quasi-steady theory for the flow through the glottis, J. Sound Vib. 276 (3) (2004) 475–490.
[15] N. Ruty, X. Pelorson, A. Van Hirtum, I. Lopez, A. Hirschberg, An in-vitro setup to test the relevance and the accuracy of low-order vocal folds models, J. Acoust. Soc. Am. 121 (1) (2007) 479–490.
[16] C.S. Peskin, The immersed boundary method, Acta Numer. 11 (2002) 479–517.
[17] B.E. Griffith, Immersed boundary model of aortic heart valve dynamics with physiological driving and loading conditions, Int. J. Numer. Methods Biomed. Eng. 28 (3) (2012) 317–345.
[18] B. Wu, The influence of the cross section shape on channel flow: modeling, simulation and experiment (Ph.D. thesis), Grenoble University, 2014.
[19] B.E. Griffith, X.Y. Luo, Hybrid finite difference/finite element version of the immersed boundary method. (submitted for publication), 2016.
[20] B. Wu, A. Van Hirtum, X.Y. Luo, Pressure driven steady flow in constricted channels of different cross section shapes, Int. J. Appl. Mech. 5 (1) (2013) 1–19.
[21] X. Grandchamp, Y. Fujiso, B. Wu, A. Van Hirtum, Steady laminar axisymmetrical nozzle flow at moderate Reynolds numbers: modeling and experiment, J. Fluid Eng.-Trans. ASME 134 (1) (2012) 1–13.
[22] X. Grandchamp, A. Van Hirtum, X. Pelorson, Hot film/wire calibration for low to moderate flow velocities, Meas. Sci. Technol. 21 (11) (2010) 115402.